Title

Cryo-EM structures of the D290V mutant of the hnRNPA2 low-complexity domain suggests how D290V affects phase separation and aggregation.

Journal

Journal of Biological Chemistry, 300(2)

Authors

Lu, Jiahui
Ge, Peng
Sawaya, Michael
et al.

Publication Date

2023-12-09

DOI

10.1016/j.jbc.2023.105531

Peer reviewed

JBC RESEARCH ARTICLE

Cryo-EM structures of the D290V mutant of the hnRNPA2 low-complexity domain suggests how D290V affects phase separation and aggregation

Received for publication, August 16, 2023, and in revised form, November 8, 2023 Published, Papers in Press, December 9, 2023,
https://doi.org/10.1016/j.jbc.2023.105531

Jiahui Lu[1,2], Peng Ge[1,2], Michael R. Sawaya[1,2], Michael P. Hughes[3], David R. Boyer[1,2], Qin Cao[4], Romany Abskharon[1,2], Duilio Cascio[1,2], Einav Tayeb-Fligelman[1,2], and David S. Eisenberg[1,2,*]

From the [1]Departments of Chemistry and Biochemistry and Biological Chemistry, University of California, Los Angeles, Los Angeles, California, USA; [2]UCLA-DOE Institute, Molecular Biology Institute, Howard Hughes Medical Institute, Los Angeles, California, USA; [3]Department of Cell and Molecular Biology, St Jude Children's Research Hospital, Memphis, Tennessee, USA; [4]Bio-X Institutes, Key Laboratory for the Genetics of Developmental and Neuropsychiatric Disorders, Ministry of Education, Shanghai Jiao Tong University, Shanghai, China

Reviewed by members of the JBC Editorial Board. Edited by Ursula Jakob

Heterogeneous nuclear ribonucleoprotein A2 (hnRNPA2) is a human ribonucleoprotein that transports RNA to designated locations for translation *via* its ability to phase separate. Its mutated form, D290V, is implicated in multisystem proteinopathy known to afflict two families, mainly with myopathy and Paget's disease of bone. Here, we investigate this mutant form of hnRNPA2 by determining cryo-EM structures of the recombinant D290V low complexity domain. We find that the mutant form of hnRNPA2 differs from the WT fibrils in four ways. In contrast to the WT fibrils, the PY-nuclear localization signals in the fibril cores of all three mutant polymorphs are less accessible to chaperones. Also, the mutant fibrils are more stable than WT fibrils as judged by phase separation, thermal stability, and energetic calculations. Similar to other pathogenic amyloids, the mutant fibrils are polymorphic. Thus, these structures offer evidence to explain how a D-to-V missense mutation diverts the assembly of reversible, functional amyloid-like fibrils into the assembly of pathogenic amyloid, and may shed light on analogous conversions occurring in other ribonucleoproteins that lead to neurological diseases such as amyotrophic lateral sclerosis and frontotemporal dementia.

Multisystem proteinopathy (MSP) consists of a related group of dominantly inherited degenerative disorders including cognitive impairment, myopathy, Paget's disease of bone and motor neuron disease (1). Mutations leading to MSP were first recognized in the valosin-containing protein gene in 2004 (2). Then in 2013, MSP patients were found bearing missense mutations in the low complexity domain (LCD) of heterogeneous nuclear ribonucleoproteins A2 and A1 (hnRNPA2, D290V; hnRNPA1, D262V) and no valosin-containing protein mutations (3). In two MSP-affected families, muscle biopsies showed that hnRNPA2 was absent from nuclei where it normally resides and instead accumulated as fibrils in cytoplasmic inclusions (3). This nuclear clearance and cytoplasmic inclusion phenomenon are also observed for ribonucleoproteins fused in sarcoma (FUS) (4) and TAR DNA-binding protein 43 (TDP-43) (5, 6).

The human hnRNPA2 belongs to a family of hnRNPs and is expressed in cells such as neurons, oligodendrocytes, and myocytes (3, 7). hnRNPA2 functions in maintaining RNA metabolism through two functionally distinct domains, the RNA-binding domain and the LCD. hnRNPA2 can bind a variety of RNA/DNA sequences (8), such as those encoding the A2 response element of the myelin basic protein (9) and transport it to targeted locations for translation by forming membraneless organelles (MLOs). hnRNPA2 was studied in RNA transport granules in oligodendrocytes (9) and stress granules in neurons (3). Its LCD was also found to undergo phase separation to form liquid droplets similar to cellular MLOs (10, 11). Studies of protein phase separation, including with FUS, TDP-43, and T-cell intracellular antigen 1, have found that MLOs constantly exchange contents with the cellular environment and are transported between organelles or cells (4, 12–17).

The LCD of hnRNPA2 can also self-assemble into a network of amyloid-like reversible fibrils that macroscopically manifests as a hydrogel. Our previous study showed that the LCD of hnRNPA2 is rich in structural motifs termed LARKS (low-complexity amyloid-like reversible kinked segments) that enable amyloid-like assemblies having lower stability than pathogenic amyloid (18, 19). LARKS contribute to the underlying transient interactions in hydrogels (19). Using footprinting, Xiang *et al.* showed that the LCD of hnRNPA2 adopts the cross-β scaffold of LARKS in liquid droplets and in hydrogels (20).

While *in vitro* results demonstrate amyloid-like assemblies are required for hydrogel assembly, the relationship between hydrogels and *in vivo* phase separation is not known. Indeed, fibrils of WT hnRNPA2 have not yet been verified *in vivo*. Furthermore, it remains to be seen whether amyloid fibrils of WT hnRNPA2 formed *in vivo* could be pathogenic. However,

* For correspondence: David S. Eisenberg, david@mbi.ucla.edu.

the extensive reversibility of WT hnRNPA2 fibrils *in vitro* (9, 21) suggests WT fibrils would likely be reversible *in vivo* and thus less likely to cause damage to cells.

So far, over 60 mutations have been identified within the LCDs of ribonucleoproteins that are associated with neurodegenerative diseases such as amyotrophic lateral sclerosis. Understanding the structure–function relationships of mutated LCDs can better assist in understanding the diseases. Identifying the disease-causing mutation D290V of hnRNPA2, Kim *et al*., used ZipperDB (22) to argue that the mutant LCD is more prone to aggregation than the WT LCD (3). In fact, they showed that the hexapeptide containing this mutated residue (NYNVFG) forms fibrils while the WT sequence (NYNDFG) does not. They also showed that recruitment of hnRNPA2 to stress granules was enhanced by the D290V mutation (3). Increased formation of cytoplasmic inclusions of the mutant hnRNPA2 was observed in mouse and *Drosophila* models and in human patients (3). Thus, structural and biochemical comparison of the WT to the mutant D290V hnRNPA2 LCD is likely to suggest how a missense mutation diverts function to pathology.

Here, we illustrate how a missense mutation diverts hnRNPA2 LCD from forming functional fibrils to forming pathogenic fibrils, and we propose four structural mechanisms to explain observations of the mutant's clearance from the nucleus and formation of cytoplasmic inclusions. We support our mechanisms with evidence from phase separation studies, thioflavin-T (ThT)-monitored kinetics of fibril formation, assays of thermostability, negatively stained EM images, and three cryo-EM structures of the mutant D290V hnRNPA2 LCD fibrils.

Results

hnRNPA2 LCD undergoes phase separation, and the D290V mutant forms aggregates faster than WT hnRNPA2-LCD

Previous studies have shown that WT hnRNPA2 LCD can undergo phase separation (10, 11). Here, we investigate whether the mutant can also undergo phase separation and whether its biophysical behavior differs from WT using recombinant hnRNPA2 LCDs. Due to its high aggregation propensity, we initially dissolved the hnRNPA2 LCD in 5.7 M guanidinium hydrochloride (GnCl). Both the WT and the mutant rapidly underwent phase separation upon dilution to a final concentration of 100 μM GnCl. The mutant liquid droplets (mean diameter: ∼1.8 μm, representative of the whole well) are half the diameter of WT droplets (mean. diameter: ∼3.4 μm) (Fig. 1*A*). We then performed "aging" experiments in which the behaviors of both constructs were monitored over time. The WT liquid droplets stayed dynamic for 24 h during which they settled to the bottom of the plate and fused into larger droplets (Fig. 1*A*, top), and then hardened into a hydrogel-like state with spiky aggregates after 48 h. In contrast, the mutant formed aggregates that look like fibrils within 3 h (Fig. 1*A* and bottom; Movie S1). We then recorded negatively stained EM of different time points of both WT and the mutant phase separation. For the D290V mutant, in the first hour, only small droplets could be seen (Fig. 1*B*, bottom). For the following 1 to 1.5 h, aggregates emanated from the droplets and connected with nearby droplets, making a dense fibrous network (Fig. 1*B*, bottom). No fibrous aggregates were observed for WT even after 48 h (Fig. 1*B*, top).

Aggregates emergent from the mutant liquid phase are partially irreversible and ThT-positive

To investigate the structural properties of the phase separation of both constructs, immediately after phase separation we added ThT, a fluorescent amyloid dye that changes conformation and fluoresces at wavelength 482 nm when it binds to cross-β structures (23). Both constructs underwent phase separation rapidly, indicating the ThT does not affect their ability to phase separate. The mutant liquid droplets showed ThT signal immediately after forming, the signal grew stronger with time, and after 4 h, a strong ThT signal was seen, and in some places in the dropletsthe aggregates grew so large that the fibril-like outline can be recognized in the fluorescence channel (Fig. 2*B*). Unlike the mutant, the WT did not show ThT signal at 10 min after liquid droplet formation. After 4 h, ThT signal was seen in the WT liquid droplets (Fig. 2*A*). The phase separation behavior we observed in the first 10 min indicates that the mutant hnRNPA2 LCD forms cross-β structure in the liquid droplets faster than WT.

We then evaluated the reversibility of the 24 h WT liquid droplets and the mutant aggregates by performing a thermostability assay. The WT and mutant samples were heated to 55 °C, the temperature at which WT hnRNPA2 hydrogel melts (18), and subsequently cooled to 4 °C. When heated, the mutant aggregates were unchanged until 55 °C when some of the aggregates melted and reformed small liquid droplets (Fig. S1, top). In contrast, the hardened WT liquid droplets were completely melted at 55 °C and dynamic small droplets were observed (Fig. S1, bottom). When cooled to 4 °C, the mutant reformed aggregates that were undisturbed by pipetting, whereas the WT liquid droplets lost their hydrogel-like characteristics and maintained liquid properties in line with its behavior stated in the earlier section (Fig. S1). Namely, "de-aged" WT liquid droplets regain normal liquid properties and harden after a prolonged time.

Phase separation of the mutant hnRNPA2 is less sensitive to pH changes than WT

To test whether phase separation of either construct is sensitive to pH, we conducted phase separation experiments at six different pH values ranging from 1.3 to 10.0. Liquid droplets of both constructs with the addition of ThT were incubated at room temperature for 22 h.

WT hnRNAP2 aggregation morphology varied notably with pH. Values near physiological pH (5.5, 7.5, and 9.0) produced droplet-shaped gels, exhibiting a strong ThT fluorescence signal under the microscope (Fig. S2*A*). However, at extreme acidic pH values such as pH 1.3 and pH 4.1, WTaggregates appear as spikes (perhaps fibrous) protruding from an amorphous center; the centers and the spikes are

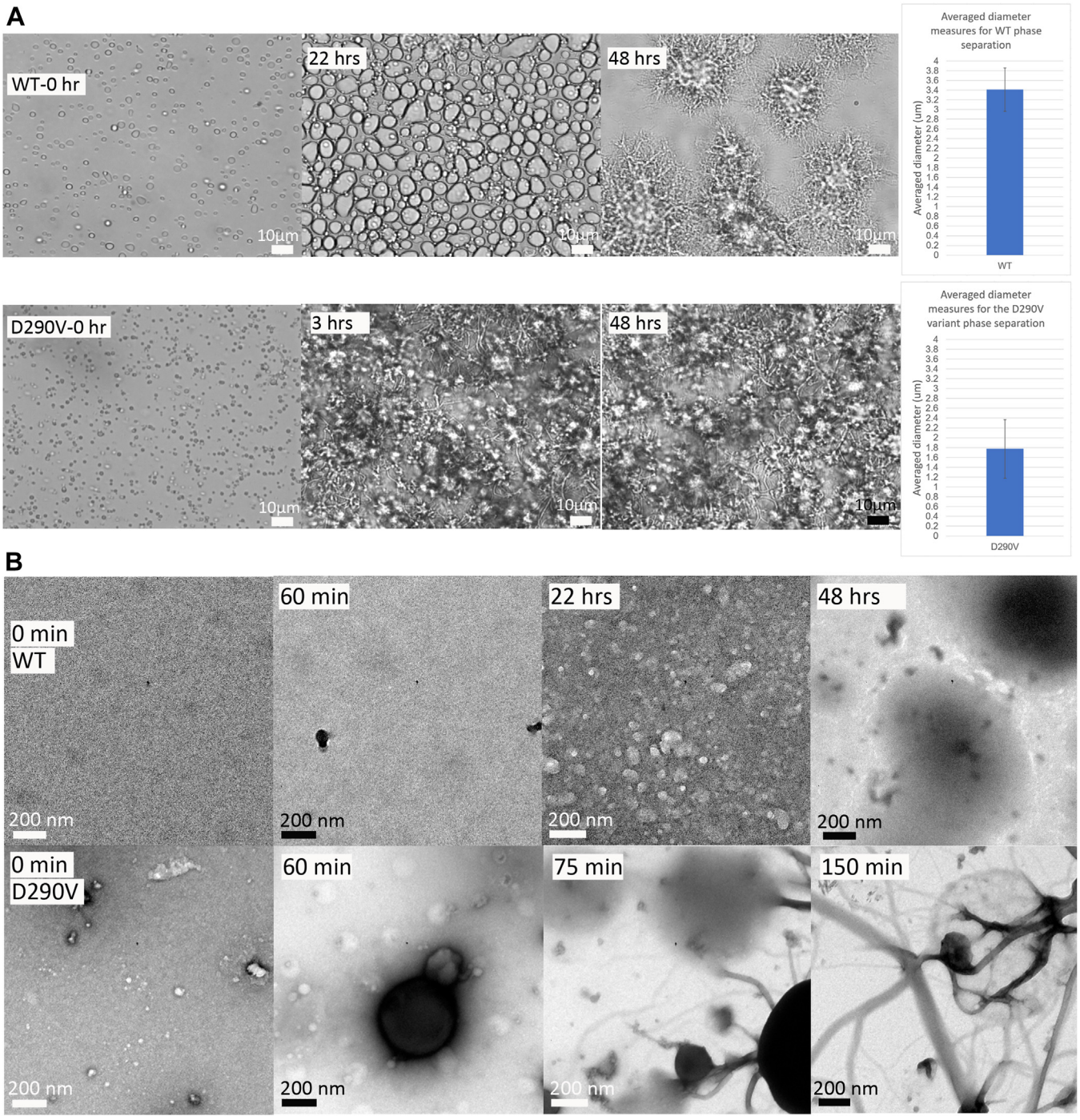

Figure 1. Phase separation of hnRNPA2 LCD and its aggregation. *A*, images were taken using differential interference contrast microscopy (DIC). The scale bar represents 10 μm. *Top panel*: phase separation of WT hnRNPA2 LCD at time points of 0 h, 22 h, and 48 h. *Rightmost* is a quantification of averaged diameter of WT liquid droplets at 1 h timepoint. *Bottom panel*: phase separation of the mutant D290V hnRNPA2 LCD at time points of 0 h, 3 h, and 48 h. Branched aggregates were observed for the mutant at much earlier time points than for the WT. *Rightmost* is a quantification of averaged diameter of the D290V mutant liquid droplets observed in the *left panel* at 1 h timepoint. *B*, negative stain EM images of hnRNPA2 LCD phase separation at different time points. The scale bar represents 200 nm. *Top panel*: WT hnRNPA2 LCD phase separation at time points of 0 min, 60 min, 22 h, and 48 h. *Bottom panel*: the D290V mutant hnRNPA2 LCD phase separation at time points of 0 min, 60 min, 75 min, and 150 min. hnRNPA2, heterogeneous nuclear ribonucleoprotein A2; LCD, low complexity domain.

both ThT-positive. In contrast to these aggregates the droplets formed at pH 10 appeared smooth and round like a liquid, but their resistance to being stirred and mixed indicated that they are actually gel-like solids (Fig. S2*A*). These alkaline aggregates, like the aggregates at lower pH values, exhibited intense ThT signal, suggesting cross-β structure is present at all pH values despite the different morphologies of the aggregates.

The mutant's aggregation morphology appeared more uniform across pH values than did WT. The mutant formed

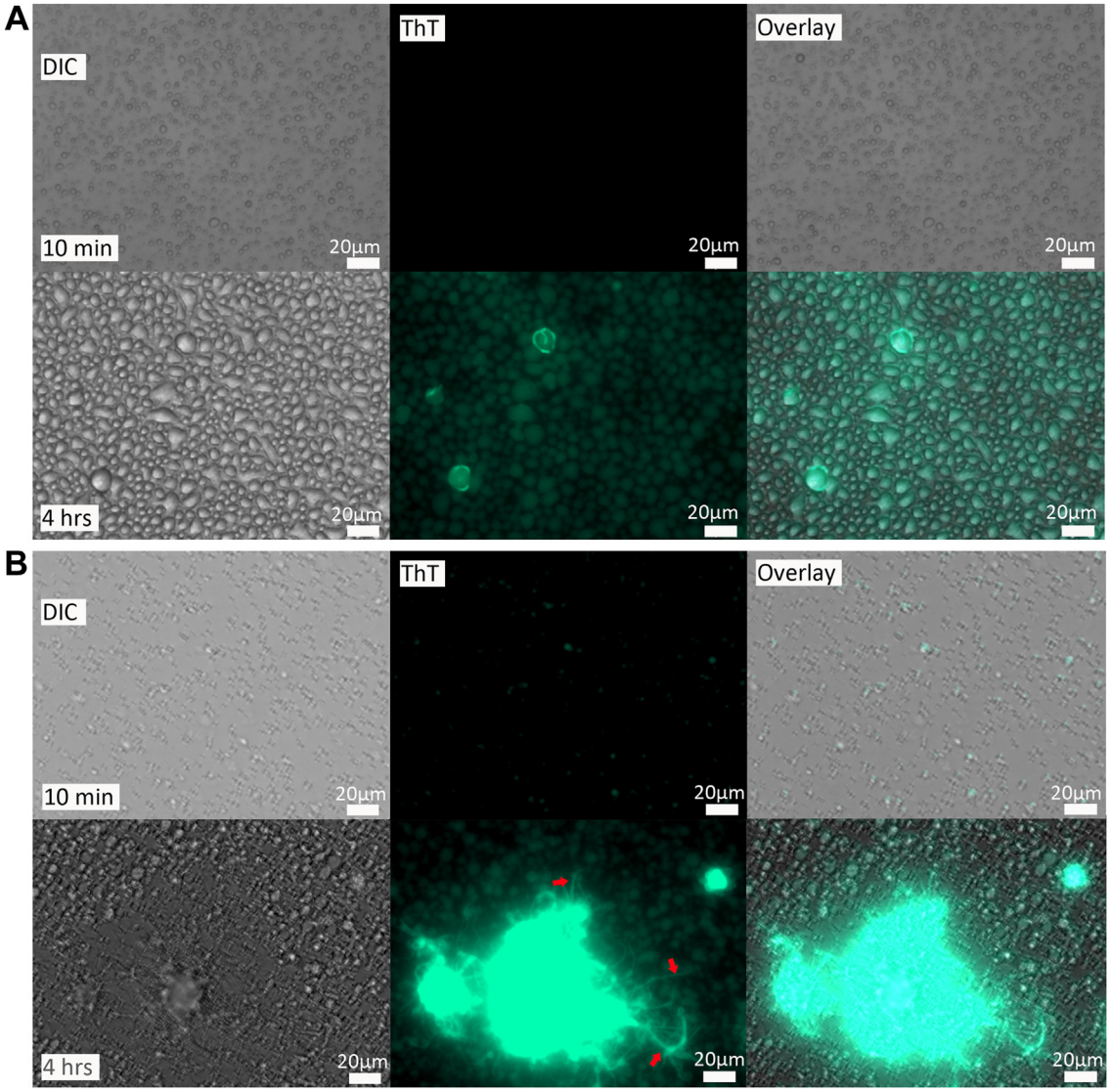

Figure 2. Phase separation of hnRNPA2 LCD is ThT-positive. Phase separation images of hnRNPA2 LCD taken by differential interference contrast (DIC) microscopy (Zeiss). *Left panel* is phase contrast channel image (DIC), *middle panel* is BO-PRO-1 channel image (BO-PRO-1 channel has an excitation and emission of 462 nm and 482 nm, respectively. We use it for ThT), *right panel* is the overlay of DIC and ThT. *A*, WT hnRNPA2 LCD phase separation at time points of 10 min and 4 h. The scale bar represents 20 μm *B*, the mutant D290V hnRNPA2 LCD phase separation at time points of 10 min and 4 h. *Red arrows* show the outlines of fibril-looking aggregates. The scale bar represents 20 μm. hnRNPA2, heterogeneous nuclear ribonucleoprotein A2; LCD, low complexity domain; ThT, thioflavin-T.

fibrous ThT-positive aggregates at all pH values sampled (Fig. S2*B*), not just at low pH values as did the WT (Fig. S2*A*). Some differences in robustness of aggregation are evident when comparing the mutant aggregation at low and high pH values; droplets of the mutant fused and aggregated faster at acidic pH than basic pH (Fig. S2*B*). Nevertheless, the conservation of morphology across all pH values indicates that aggregation of the mutant hnRNPA2 LCD is less sensitive to pH changes than WT.

Fibrils of the mutant grow faster and are more stable than fibrils of WT hnRNPA2 LCD

We compared fibril growth kinetics and thermodynamics of WT and the mutant hnRNPA2 LCD produced recombinantly. The LCDs of WT and mutant were individually dissolved in buffer containing 20 mM Mops, pH 7.5, 150 mM KCl buffer and 2 M GnCl to a final concentration of 4 to 5 mg ml^{-1} and was shaken at 4 °C for 3 days. ThT assays showed that the mutant formed fibrils after 20 min whereas WT formed fibrils after 25 h (Fig. 3*A*). WT hnRNPA2 LCD fibrils remain intact up to 45 °C, but completely melt at temperatures 55 °C and above (Fig. S3), consistent with our previously reported results (18). The mutant hnRNPA2 LCD fibrils, however, remain intact until 55 °C, and do not melt until 65 °C (Fig. 3*B*). Upon cooling to 4 °C, both the mutant and the WT hnRNPA2 LCDs reform fibrils (Figs. 3*B* and S3).

Cryo-EM reveals the PY-NLS is buried in all three fibril polymorphs of the mutant hnRNPA2-LCD

Atomic-resolution structures of amyloid fibrils of both mutant and WT hnRNPA2 LCDs are essential for

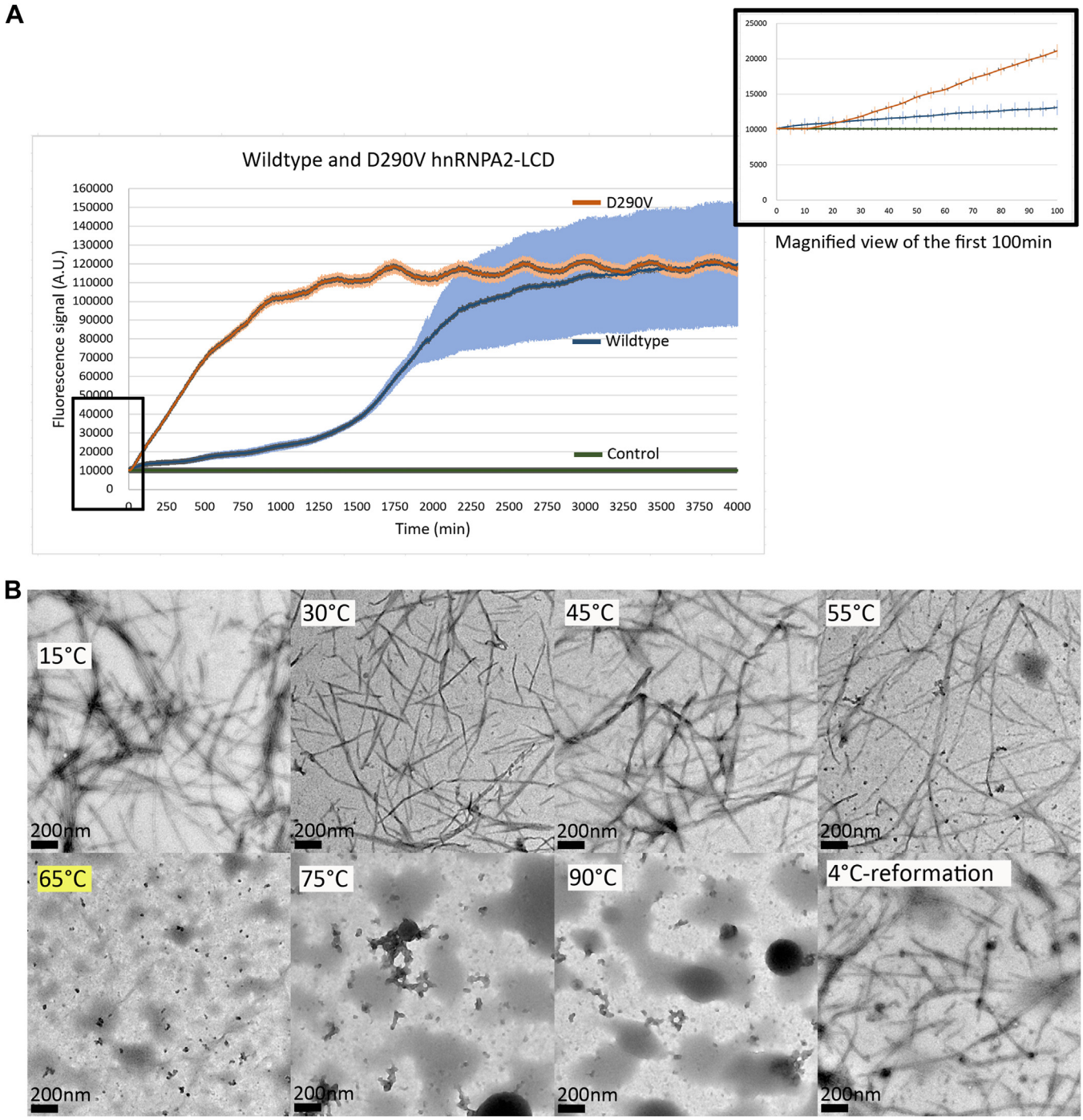

Figure 3. ThT and thermostability assays of hnRNPA2 LCDs. *A*, ThT assay of WT and the mutant D290V hnRNPA2 LCDs. *X*-axis represents time in the unit of minutes, *Y*-axis represents fluorescence signal. The WT ThT curve is colored *blue*, the mutant ThT curve is colored *orange*, the control ThT curve with buffer only is colored *green*. The box shows a magnified view of the first 100 min of the ThT curve. *B*, representative negative stain EM images of the thermostability assay of the mutant D290V hnRNPA2 LCD. The mutant fibrils are melted at 65 °C, which is colored *yellow* to highlight this transition. The scale bar represents 200 nm. hnRNPA2, heterogeneous nuclear ribonucleoprotein A2; LCD, low complexity domain; ThT, thioflavin-T.

understanding why the mutant accumulates in the cytoplasm, not the WT. The fibril structure of WT hnRNPA2-LCD has been determined and described previously (18). Here, we collected cryo-EM data on fibrils of the D290V mutant. During data collection and 3D classification, we found a total of six polymorphs (PMs), yet only three of them (PM1-3) had a sufficient number of particles to be determined to near-atomic resolution (Fig. S4). Contrary to globular proteins which fold into 3D shapes, molecules of the mutant hnRNPA2 LCD are confined to 2D layers in each of the three fibril PMs. These layers stack on top of identical layers, forming a twisted, in-register β-sheet that runs parallel to the fibril axis. The details of the three polymorphic fibrils are as follows.

(1) PM1 consists of two protofilaments with pseudo-2_1 screw symmetry, and is determined to a resolution of 3.3 Å. The fibril is a left-handed helix with a pitch of 2335 Å, giving rise to a helical twist of 179.63° and a rise of 2.40 Å. Out of 161 residues in the LCD, 54 residues, from Gly263 to Gly316, form the fibril core. The fibril core contains the disease-causing D290V mutation which is solvent exposed, and half of the PY-nuclear localization signal (PY-NLS). The PY-NLS is a 19-residue segment extending from Tyr301 to Tyr319 (24); 16 of the 19 residues (Tyr301 to Gly316) are ordered in the mutant structures. The remaining three residues of the PY-NLS and 107 LCD residues are disordered in the "fuzzy coat". The interface between the two protofilaments spans residues Tyr294 to Gly311. The rest of the C-terminal residues are the PY-NLS (Fig. 4*B*).

(2) PM2 is structurally similar to PM1. It also consists of two protofilaments with pseudo-2_1 screw symmetry and is determined to a resolution of 3.2 Å. It is a left-handed fibril with a pitch of 2151 Å, giving rise to a helical twist of 179.60° and a rise of 2.39 Å. The same 54 residues from Gly263 to Gly316 form the fibril core, with the disease-causing D290V mutation exposed to the solvent on the outer surface. The core adopts the same fold as PM1, but PM2 has a smaller and more interdigitated interface between the two protofilaments involving residues Tyr294 to Pro303 (Fig. 4*C*).

(3) PM3 has C1 symmetry and is determined to a resolution of 3.9 Å. PM3 is a left-handed fibril consisting of three protofilaments with a pitch of 2390 Å, giving rise to a helical twist of −0.72° and a rise of 4.78 Å. Due to the limited resolution of the PM3 map, we restricted our refinement of PM2 to rigid body fitting, rather than allowing individual atomic refinement. All three chains span 54 residues from Gly263 to Gly316. The disease-associated mutation D290V of chain A and chain B are solvent exposed on the fibril outer surface. V290 of chain C is buried by van der Waals interactions with Asn293 and Tyr294 of chain B. (Fig. 4*D*). We acknowledge that the resolution of this map is limited, especially for chain B.

All three PMs have a buried PY-NLS where Arg313 is hidden within the fibril core (Fig. 5, *A*–*C*). Data and atomic refinement statistics of all three PMs are summarized in Table 1.

The fibril core is necessary for hnRNPA2 phase separation

Both WT and mutant hnRNPA2 LCD fibril cores span a similar sequence range (Gly263-Tyr319 (18) and Gly263-Gly316, respectively). To test the importance of the fibril core in phase separation, we generated a construct of 104 residues of hnRNPA2 LCD without the 57-residue fibril core. Under the conditions that produced phase separation in full-length hnRNPA2, the deletion mutant did not undergo phase separation (Fig. S5). We thus argue that the residues defining the fibril core are essential for hnRNPA2 phase separation.

The mutant structures are energetically more stable than the WT hnRNPA2-LCD

To quantify the structural features that lead to a more stable mutant conformation, we calculated the atomic solvation energy of the PM1-3 fibril structures and compared the values to the WT. We obtained the solvation energy per layer of the fibril and an average solvation energy per residue. We illustrated these energies in a solvation energy map where each residue is colored according to its energy. The solvation energy per layer of the WT (−22 kcal mol^{-1} per layer) has a less negative value than all three PMs of the mutant (PM1: −28 kcal mol^{-1} per layer; PM2: −37 kcal mol^{-1} per layer; PM3: −55 kcal mol^{-1} per layer), indicating the WT structure is less stable on a per-layer basis than the mutant structures (Fig. 6).

The mutant structures have an increased number of β-sheet residues

Steric zippers are pairs of β-sheets where the sidechains mate tightly with each other in a dry interface. Steric zippers are highly energetically stable and are commonly found in pathogenic amyloids (25). We compared the number of residues having phi and psi angles within the β-sheet regions of the Ramachandran plots of both WT and the mutant structures. We categorized three residue types: S for residues in the β-sheet region, H for residues in either left-handed or right-handed α-helix region, and O for other residues that are neither β-sheet nor α-helix. We found an increased number of S residues (WT: 47%, PM1: 56%, PM2: 67%, and PM3: 67%) and a decreased number of O residues (WT: 35%, PM1: 26%, PM2: 18%, and PM3: 18%) in all three PMs of the mutant, and a similar percentage of H residues (Fig. S6). The mutant structures adopt more steric zipper motifs, namely, more β-sheet residues, than the WT which lead to their increased stability.

Discussion

Disease relevance of the structures of the D290V variant of hnRNPA2 low-complexity domain

Advances in cryo-EM capabilities have enabled structure determination of amyloid fibrils extracted from various organs, including brain, kidney, and heart. About one third of the amyloid structures determined to date (85/232) originate from *ex vivo* samples (26). The majority; however, originate from recombinant material. For central nervous system-related diseases, for which structures exist from both *ex vivo* and *in vitro* samples, structural differences can be substantial. In other cases, close similarities can be found, extending over the entire fold (Fig. S7, *A*–*D*), or subregions (Fig. S7, *E*–*H*) Accordingly, caution is necessary in ascribing relevance to disease of our structure of recombinant D290V variant hnRNPA2, which is associated with MSP. In the case of MSP, the chance of faithfully reproducing disease-relevant fibrils *in vitro* may be greater than the faithful reproduction of disease-relevant fibrils of age-related central nervous system conditions such as Alzheimer's and Parkinson's. MSP, has an

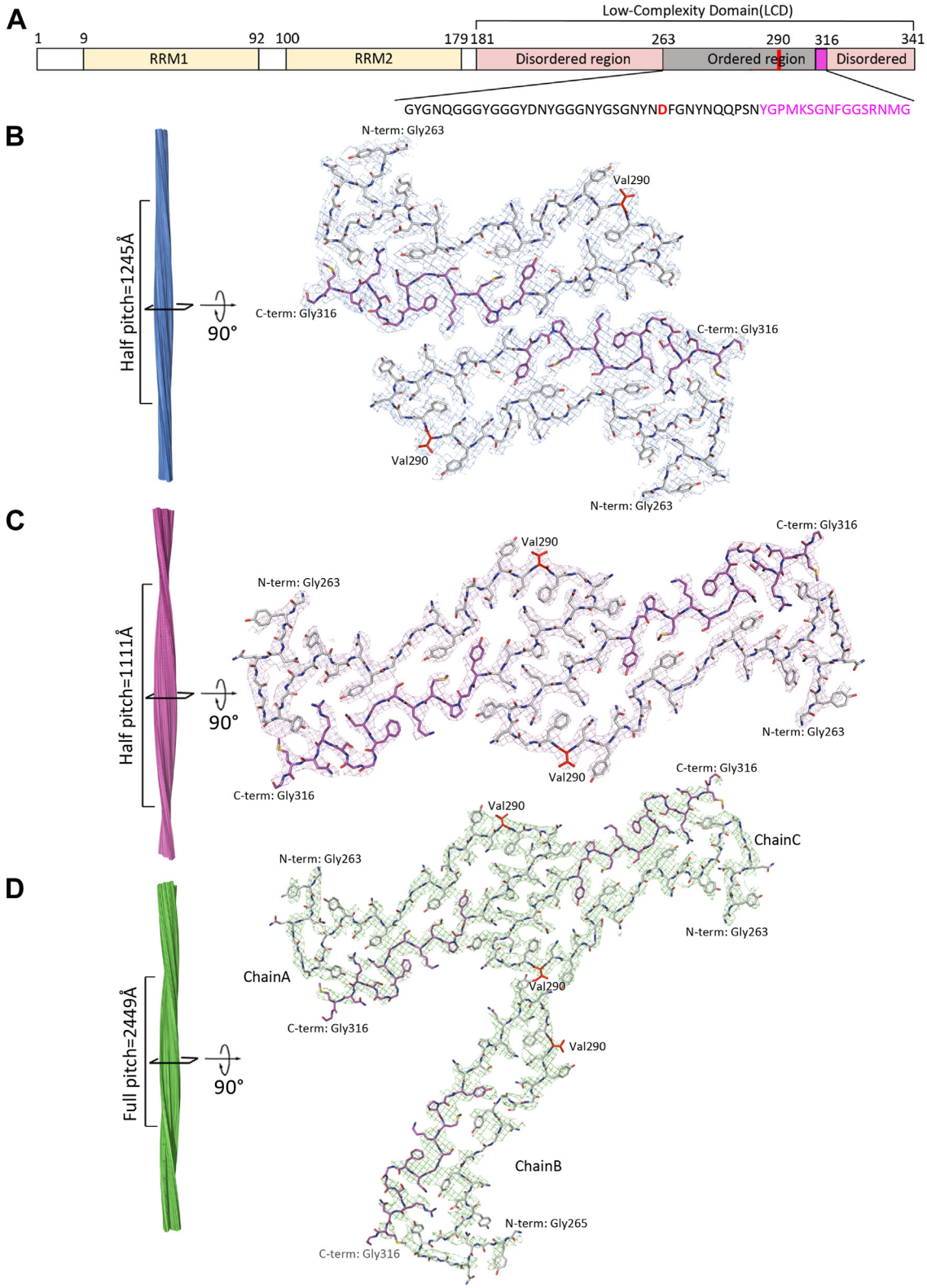

Figure 4. The cryo-EM structures of the mutant D290V hnRNPA2 LCD fibril cores. *A*, domain structure of full-length hnRNPA2. The LCD (residues 181–341) was used for fibril structure determination. The *gray bar* shows the range of the residues that form the ordered fibril core of the cryo-EM structure. The *red bar* shows the disease-causing mutation. The *magenta bar* shows the PY-NLS. The sequence of the ordered region is shown below with corresponding colors. *B–D*, (*B–D*) are PM1, PM2, and PM3, respectively. *Left*: fibril reconstruction showing left-handed pitch and twist. *Right*: density and atomic model of one cross-sectional layer of each fibril. Disease-causing mutation is colored *red*, and PY-NLS residues are colored *magenta*. N-term: N terminus; C-term: C terminus. hnRNPA2, heterogeneous nuclear ribonucleoprotein A2; LCD, low complexity domain; NLS, nuclear localization signal; PM, polymorph.

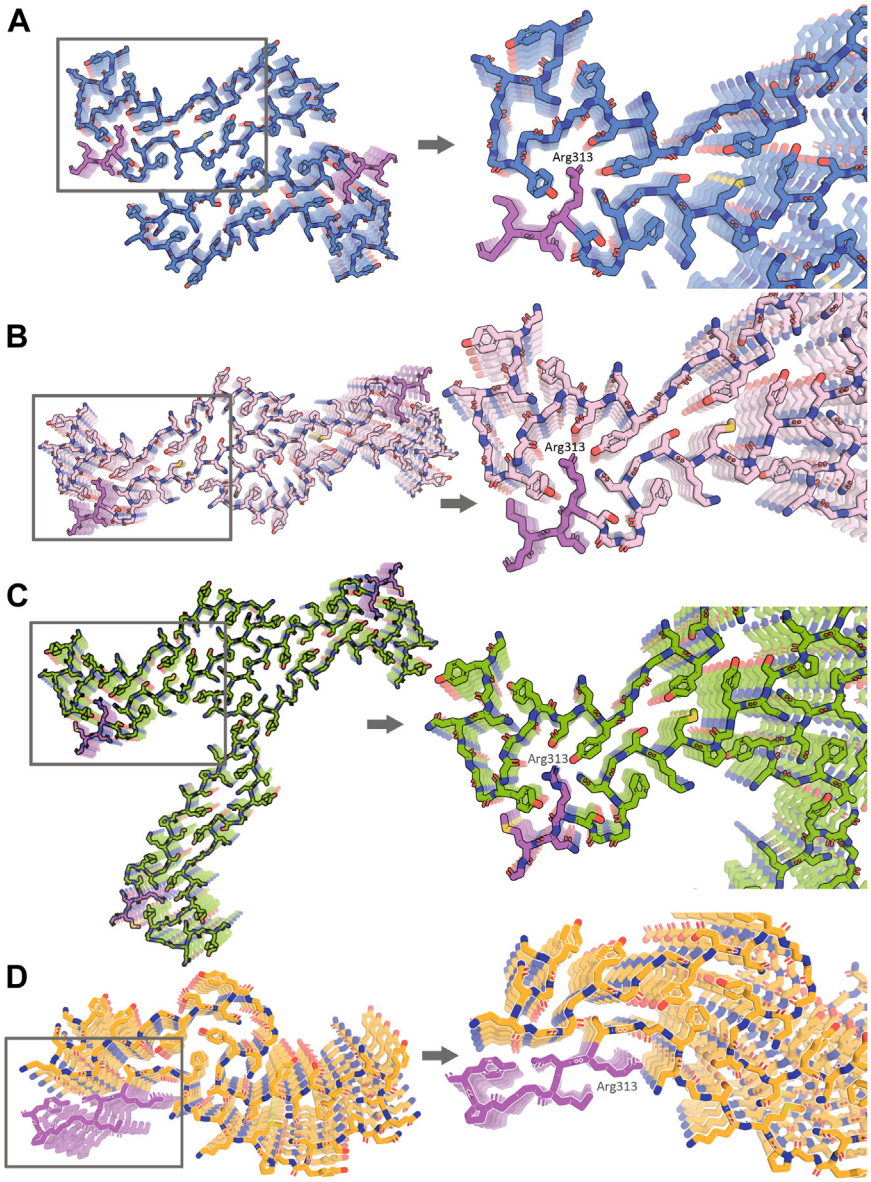

Figure 5. Unlike WT, the conserved Arg313 of the PY-NLS is hidden in all three morphologies of the mutant hnRNPA2. *A–D*, cryo-EM structure of PM1-3 and WT hnRNPA2, respectively, zoomed in region of the $RX_{2\text{-}5}PY$ motif of PY-NLS (colored *magenta*) is shown on the *right*, corresponding to the *gray* box on the *left*. hnRNPA2, heterogeneous nuclear ribonucleoprotein A2; NLS, nuclear localization signal; PM, polymorph.

age of onset of about 20, which is about half that of Alzheimer's disease. The shorter incubation time for fibril formation may be easier to simulate in a test tube. Moreover, the hnRNPA2 sequence may have evolved to resist amyloid polymorphism; WT hnRNPA2 yields only a single definite structure, whereas pathogenic brain amyloids, such as WT tau and α-synuclein, adopt several different PMs when elicited *in vitro*.

Relative stability of WT and mutant hnRNPA2 LCD fibrils

We found that the mutant D290V hnRNPA2 LCDs are more stable than the WT, as judged both biochemically and computationally, by the following reasons.

(1) The emergence of aggregates from the fused liquid droplets of the mutant hnRNPA2 is faster than WT. Although both WT and the mutant form aggregates after 48 h, the mutant forms ThT-positive aggregates much faster and more macroscopically obvious than WT. We observed that, after 2 to 3 h, the mutant hnRNPA2 LCD forms partially irreversible ThT-positive, fibrous aggregates from its fused liquid droplets. In contrast, after 24 h the WT droplets remain gel-like and reversible. The mutant shows ThT fluorescence immediately when the liquid droplets form and the signal strengthens as the aggregates grow, indicating that some of the mutant hnRNPA2 LCDs adopt cross-β structures shortly after the droplets form and over time they assemble into cross-β-rich aggregates. That WT droplets fail to display ThT signal until hours later suggests that cross-β structures form gradually in the liquid droplets. We cannot rule out the possibility that the ThT fluorescence from the droplets may result from an over concentration of ThT. But

Table 1
Statistics of cryo-EM data collection, refinement, and validation

	#1 PM1 (EMDB-277133) (PDB 8DU2)	#2 PM2 (EMDB-27728) (PDB 8DUW)	#3 PM3 (EMDB-28014) (PDB 8EC7)
Data collection and processing			
Magnification	X81,000	X81,000	x81,000
Voltage (kV)	300	300	300
Electron exposure (e–/Å^2)	36	36	36
Defocus range (μm)	0.5–5.0	0.5–5.0	0.5–5.0
Pixel size (Å)	1.1	1.1	1.1
Symmetry imposed	C1/P2$_1$	C1/P2$_1$	C1
Initial particle images (no.)	128565	197905	171774
Final particle images (no.)	5675	14902	16114
Map resolution (Å)	3.3	3.2	3.9
FSC threshold	0.143	0.143	0.143
Helical rise (Å)	2.40	2.39	4.78
Helical twist (°)	179.63	179.60	–0.72
Map resolution range (Å)	200–3.3	200–3.2	200–3.9
Refinement			
Initial model used (PDB code)	*De Novo*	*De Novo*	Rigid body of PM2
Model resolution (Å)	4.0	3.4	4.5
FSC threshold	0.5	0.5	0.5
Model resolution range (Å)	200–3.6	200–3.4	200–4.2
Map sharpening *B* factor (Å^2)	108	76	51
Model composition			
Nonhydrogen atoms	3900	3900	5850
Protein residues	540	540	810
B factors (Å^2)			
Protein	79.00	59.21	109.54
R.m.s. deviations			
Bond lengths (Å)	0.003	0.006	0.002
Bond angles (°)	0.469	0.514	0.393
Validation			
MolProbity score	1.39	1.55	1.36
Clashscore	7.17	5.34	6.47
Poor rotamers (%)	0.00	0.00	0.00
Ramachandran plot			
Favored (%)	98.08	96.15	98.08
Allowed (%)	1.92	3.85	1.92
Disallowed (%)	0.00	0.00	0.00
CC (mask) model *versus* data	0.81	0.83	0.67

EMDB, Electron Microscopy Data Bank; PDB, Protein Data Bank.

we believe the aggregates from the mutant droplets corroborate our idea that there is cross-β structure in the droplets. However, further experiments involving determining the structure of those mutant aggregates are required because they are prepared differently.

At 24 h, the aggregation we observed in the WT droplets resembles what we previously observed, a hydrogel composed of a dense fibril network that is heat-reversible (18). That the WT droplets maintain the droplet shape, are ThT-positive, and are reversible by heating indicates that the WT droplets form hydrogels. We think the probability for droplets being seeded by small aggregates from the bulk solution is low because the sample was centrifuged to get rid of aggregates before the phase separation assay. But we admit that we do not have sufficient data to substantiate the sequence of events regarding phase separation and fibril formation. That we do not see fibrous networks in WT gel-like droplets, as we have seen for hydrogels by negatively stained EM suggests that phase separation and fibril formation might not necessarily be related. Overall, our results from ThT and phase separation assays imply that the mutant hnRNPA2 LCD has stronger and more stable intramolecular and intermolecular interactions than the WT.

(2) The mutant hnRNPA2 LCD forms fibrils with a much shorter lag time (∼20 min) and melts at a higher temperature (65 °C) than the WT (∼25 h and 55 °C). Our results are consistent with previous evidence that, by agitation, the GST-tagged mutant hnRNPA2 LCD forms fibrils faster than the WT (3), and the mutant hnRNPA2 LCD is thermodynamically more stable than WT (27). Our results suggest that the mutant hnRNPA2 LCD more easily assembles into fibrils which are more resistant to dissociation than WT fibrils.

(3) Aggregation behavior of the mutant hnRNPA2 LCD is less sensitive to pH changes than the WT. Aggregates of mutant hnRNPA2 exhibit the same morphology over a wide pH range, unlike WT. When the pH is below 4, WT has more abundant and thicker spiky aggregates than the mutant hnRNPA2 LCD, because WT Asp290 will be protonated and less likely to form H-bonds with residues Tyr288 and Gly292 amide backbone (Fig. S8). Thus, we hypothesize that the WT may adopt an aggregated form potentially similar to the structures the mutant will adopt at physiological pHs. We conclude that both WT and the mutant hnRNPA2 LCDs phase separate and aggregate at high concentrations under physiological conditions, adopting cross-β scaffolds, with the mutant scaffold being more stable than WT, possibly because the interaction motifs of WT hnRNPA2 LCDs are mainly LARKS rather than steric zippers.

(4) The mutant hnRNPA2 fibrils are energetically more stable than WT according to solvation energy estimates calculated from hnRNPA2 LCD fibril structures. The

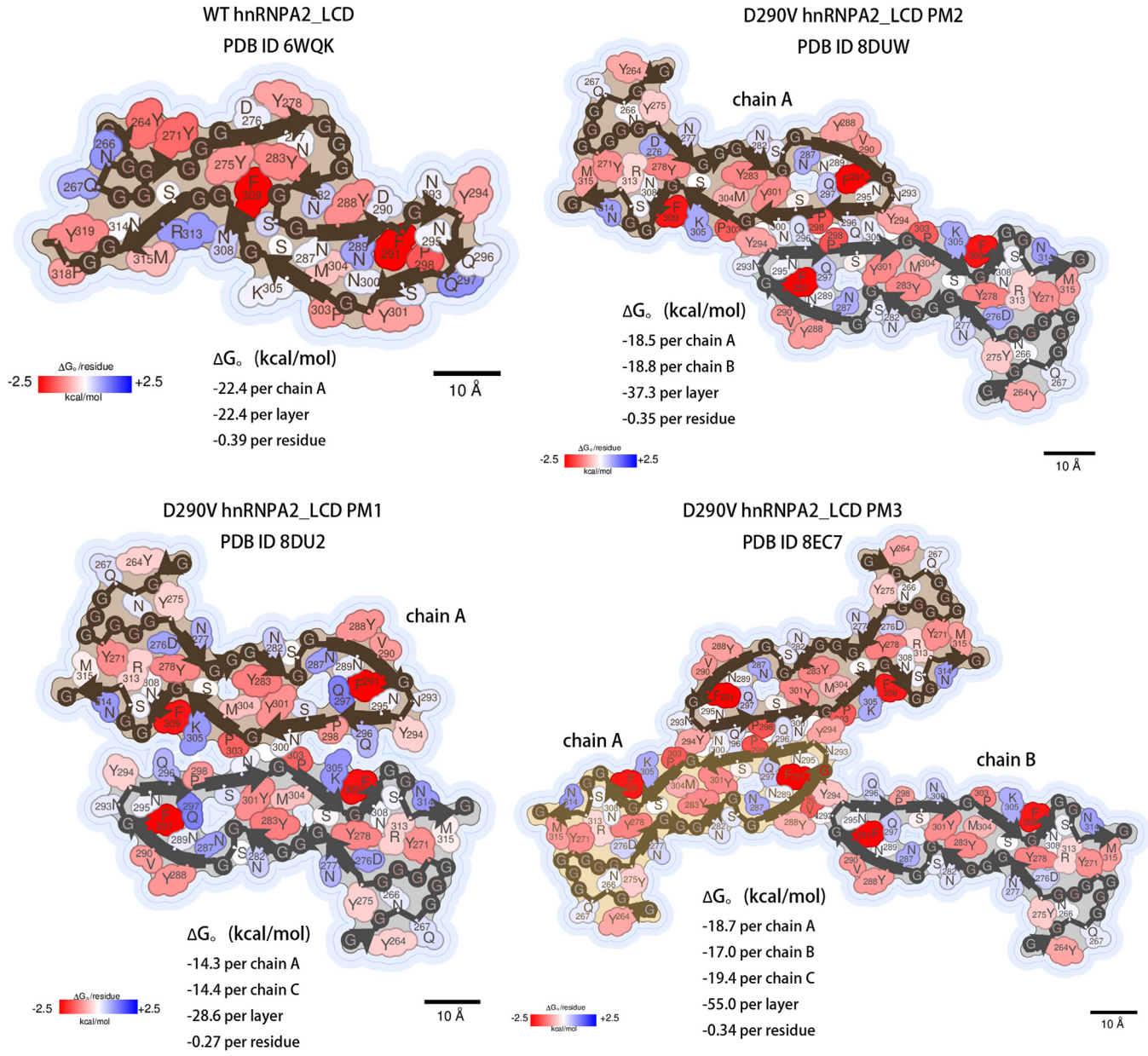

Figure 6. Calculated solvation energy maps for hnRNPA2 LCD fibrils based on atomic solvation parameters. Residues are colored according to their stabilization energies from unfavorable (*blue*, +2.5 kcal mol^{-1}) to favorable (*red*, −2.5 kcal mol^{-1}). *Top left*: WT hnRNPA2 LCD fibril core; *top right*: PM2 of the mutant hnRNPA2 LCD fibril core; *bottom left*: PM1 of the mutant hnRNPA2 LCD fibril core; *Bottom right*: PM3 of the mutant hnRNPA2 LCD fibril core. The scale bar represents 10 Å. hnRNPA2, heterogeneous nuclear ribonucleoprotein A2; LCD, low complexity domain; PM, polymorph.

calculations are consistent with our biochemical experiments. The mutant structure has a more negative value of solvation energy per layer (PM1: −28 kcal mol^{-1} per layer; PM2: −37 kcal mol^{-1} per layer; PM3: −55 kcal mol^{-1} per layer) than the WT (−22 kcal mol^{-1} per layer), indicating that it is energetically more stable and therefore requires more energy to dissociate it than the WT. The mutant structure solvation energy is in the middle of the energy spectrum in terms of solvation energy values (26), where it is not as stable as irreversible pathogenic amyloid fibrils such as human amyloid serum A (28) (−69 kcal mol^{-1} per layer) and Tau (29) (−63 kcal mol^{-1} per layer), but is much more stable than the reversible functional amyloid-like fibrils such as FUS (30) (−12 kcal mol^{-1} per layer) and WT hnRNPA2 (18) (−22 kcal mol^{-1} per layer). This implies that the higher stability of the mutant structure might not be the only reason for its accumulation in the cytoplasm.

Possible structural mechanisms of D290V mutant hnRNPA2 accumulation in the cytoplasm

Kim *et al.*, reported in 2013 that the D290V mutant hnRNPA2 is cleared out from the nucleus and forms cytoplasmic inclusions. Given the fibril structures of the WT and mutant LCDs of hnRNPA2 and their relative stabilities, what is the mechanism by which a missense mutation diverts the

assembly of reversible functional amyloid-like fibrils to assembly of irreversible pathogenic amyloid that leads to its accumulation in the cytoplasm? We ruled out the possibility that a difference in the polarity of amino acid composition of the fibril core contributes to a difference in fibril stability. The mutant and the WT hnRNPA2 LCDs have similar fibril core sequences with almost identical polar residue compositions (47% of polar residues in WT and 46% in the mutant). So, we must look further to understand the dramatic biological effect of a single missense mutation.

In the following, we propose four structural mechanisms that could explain why the D290V mutant hnRNPA2 accumulates in the cytoplasm.

(1) A loss of function for mutant hnRNPA2 arises because its PY-NLS is obscured in the fibril core, disrupting its designated nuclear localization. Unlike the WT hnRNPA2 LCD structure, all three PMs of the mutant hnRNPA2 LCD structures have a PY-NLS where the arginine residue, R313, is deeply buried in the fibril core, making it inaccessible to chaperones such as karyopherin-β2 (Kapβ2) (Figs. 4 and 5). Previous work has shown that the conserved arginine, acting as an epitope of the $RX_{2\text{-}5}PY$ motifs of PY-NLS of hnRNPA1, hnRNPD, and FUS binds to the C-terminal arch of Kapβ2 by forming a salt bridge (31–36). Thus, when R313 of hnRNPA2 is buried inside the D290V mutant fibril core, the PY-NLS loses its function because the conserved arginine can no longer interact with Kapβ2 (36) (Fig. 5). In short, the structure of the mutant fibril offers a simple mechanism by which a genetic lesion promotes development of disease.

Of importance, our D290V mutant hnRNPA2 structure reveals a difference from the WT structure that is consistent with known loss of function of the mutant: hnRNPA2 is an RNA-binding ribonucleoprotein that functions normally in mRNA transport from the nucleus to the cytoplasm and then to the designated locations for translation. However, in two families afflicted with MSP, hnRNPA2 was found in the muscle cell cytoplasm rather than in the nuclei. This loss of normal function is consistent with the salient point of our mutant structure: that the NLS is obscured, which could account for the mislocalization of hnRNPA2 in these cases. Recent studies by J. Paul Taylor's lab have shown that a frameshift in the PY-NLS of hnRNPA2 reduces its affinity to chaperone Kapβ2, leading to hnRNPA2's accumulation in the cytoplasm (37). Both their and our results show the biological significance of a fully accessible and intact PY-NLS.

There is a possibility that chaperones like Kapβ2 can also bind to the WT, because R313 of the WT is also partially tucked inside the WT structure, forming hydrogen bond with nearby G310 carbonyl group (Fig. 5*D*). We propose the hypothesis that the mutant will be much less accessible to chaperones than WT because the R313 of PY-NLS of the mutant is buried deeper in the fibril core.

(2) The D290V aggregates are somewhat more stable than the WT aggregates, as discussed in the preceding section. Compared to the WT hnRNPA2 structure, there is an increased number of residues adopting β-sheet conformations in the mutant structures. In the WT structure, the Asp290 side chain forms a Van der Waals interaction and a hydrogen bond network with the Tyr288 side chain and Gly292 backbone amide (Fig. S9). The mutant molecule losing this hydrogen bond results in Gly292 adopting a β-sheet conformation rather than a kinked conformation. Due to this loss of hydrogen bond, we noticed a number of structural differences deeper in the fold that appear linked to residue 290. Notably, the sidechains of half of all the residues flip between inward and outward facing orientations (Fig. S8*B*), and there is in an overall increase in the β-sheet content of the mutant structures compared to WT both upstream and downstream of Val290 (Fig. S6*B*). Many upstream glycine residues change into β-sheet conformation, including Gly265, 268 to 269, 272 to 273 and Gly285. Multiple downstream polar residues, including Tyr294, Gln297, Asn300, Tyr301, and Met315, also adopt β-sheet conformation in the mutant structures. Pathogenic amyloid fibrils normally have a high β-sheet content (https://srv.mbi.ucla.edu/AmyloidAtlas/) creating stability (26). We believe the stability of the mutant hnRNPA2 to be rooted in the higher β-sheet content of its LCD. Notably, a hereditary mutation resulting in a more stable α-synuclein fibril structure is posited to drive pathogenesis of a familial form of Lewy body dementia (38), indicating that production of more stable fibrils *via* missense mutations may be a common mechanism of pathogenesis in amyloid disease.

(3) The side chain of the solvent-exposed V290 disease-associated replacement presumably makes nonspecific interactions with other proteins in cells. It is unexpected to us that the disease-associated valine side chain is solvent exposed in all three mutant PMs, because burying this hydrophobic residue would make the structure more stable. In PM3 of the mutant structure, the exposed valine interacts with protofilament B. We thus speculate that the exposed valine can also have nonspecific hydrophobic interactions with other proteins or RNAs in the MLOs (39–41), resulting in a sequestration and a loss of function of other proteins. It is also notable to us that half of the inward-facing residues in the WT structure become outward-facing in the mutant structures and vice versa (Fig. S8*A*). These changes lead to new surface epitopes that could potentially contribute to the mutant's toxicity in cells.

(4) Similar to other pathogenic amyloid fibrils such as tau (29), α-synuclein (42), and islet amyloid polypeptide (43), the hnRNPA2 LCD mutant structures are polymorphic. The mutant structures are composed of two or three protofilaments with the same fold, but the protofilaments are arranged slightly different from each other (Fig. 4). PM1 differs from PM2 with an 8-residue larger interface, and PM2 differs from PM3 with an additional protofilament. The other three unsolved structures are also different arrangements of PM1/2 or PM3, with an even smaller interface or an additional protofilament interacting at

another position (Fig. S4*B*). In principle, all six PMs of the mutant hnRNPA2 LCD can have different first and second nucleation rates, fragmentation rates, and extension rates, resulting in some PMs (PM1-PM3) predominating over the others. Polymorphism can affect the self-propagation rate by providing more templates to seed and extend (44). It has been shown that different PMs of α-synuclein fibrils have different seeding capacities and cytotoxicity profiles (45). The altered nucleation and seeding rates will likely change the dynamics of RNA-containing MLOs and disrupt cellular RNA metabolism. Most functional amyloids fold into a single morphology presumably through evolution. Due to the sensitivity of amyloids to change structures under different environmental conditions or mutations, it is not surprising that D290V of hnRNPA2 leads to such a dramatic effect.

Our experiments confirm previous ideas that phase separation, hydrogel formation and fibril formation are connected events in the aggregation of both WT and mutant hnRNPA2 LCD, and probably sequential states (20, 46). Similar phenomenon are also observed for FUS (4) and TDP-43 (5, 6). Thus, our structures for both WT and mutant fibrils establish their clear differences, including monomorphic *versus* polymorphic fibrils. At the same time, we find the mutant differs from other pathogenic amyloids in that it is not as energetically stable. Our results show that the mutant hnRNPA2 LCD has an intermediate solvation energy value between functional fibrils and pathogenic amyloid, indicating that stability is not the only factor that contributes to its accumulation in the cytoplasm. We propose four mechanisms in addition to stability to explain: (1) loss-of-function by the hidden PY-NLS; (2) an increase in the β-sheet content; (3) nonspecific interactions by exposed Valine 290; and (4)) polymorphism.

In summary, comparison of the recombinant WT and recombinant D290V mutant hnRNPA2 structures offers hypotheses for how a missense mutation leads to nuclear clearance and cytoplasmic accumulations. To test our hypotheses, future research is needed on whether both the WT and the mutant hnRNPA2 can bind chaperones like Kapβ2 *in vitro* and *in vivo*.

Experimental procedures

Materials and purification of mCh-hnRNPA2 LCD fusion protein

The construct for overexpression of both the WT and the mutant mCherry-hnRNPA2-LCD fusion protein was provided by Dr Masato Kato of the University of Texas, Southwestern. A tobacco etch virus (TEV) cleavage site was inserted between mCherry and hnRNPA2 LCD. HnRNPA2 LCD without the fibril core construct was designed using benchling and ordered through Twist Bioscience.

Protein overexpression and purification procedures followed the same protocol reported previously (18). Protein was overexpressed in *E. coli* BL21(DE3) cells with 0.5 mM IPTG at 25 °C for overnight. LB media with 0.1 mg ml^{-1} ampicillin was used for cell culture. Harvested cells were resuspended in lysis buffer containing 50 mM Tris–HCl pH 8.0, 500 mM NaCl, 2 M guanidine HCl, 2 mM tris(2-carboxyethyl)phosphine (TCEP), and Halt protease inhibitor cocktail (Thermo Fisher Scientific) for 30 min on ice and then sonicated. The cell lysate was centrifuged at 32,000*g* for an hour. The supernatant was filtered and loaded onto a 5 ml HisTrap HP column (GE HealthCare) for purification. The HisTrap column was preequilibrated with the lysis buffer. After proteins were loaded onto the column, proteins were washed with the lysis buffer until the UV280 spectrum line became flat. The sample then was washed with a 20 column volume gradient at the speed of 1 ml/min from 100% wash buffer containing 25 mM Tris–HCl pH 8.0, 150 mM NaCl, 2 M GnCl, 20 mM imidazole, and 2 mM TCEP to 100% elution buffer containing 25 mM Tris–HCl pH 8.0, 150 mM NaCl, 2 M GnCl, 300 mM imidazole, and 2 mM TCEP. Purified mCherry-hnRNPA2-LCD fusion proteins were dialyzed overnight at room temperature against a dialysis buffer containing 20 mM Tris–HCl pH 7.5, 200 mM NaCl, 20 mM 2-Mercaptoethanol, 0.5 mM EDTA, and 0.1 mM PMSF. The protein solutions were concentrated to 40 to 80 mg ml^{-1} and flash frozen in liquid nitrogen and stored in −80 °C for future use.

TEV cleavage and formation of hnRNPA2 LCD fibrils

Purified and concentrated mCherry-hnRNPA2-LCD was incubated with 1:200 v/v of 10 mg ml^{-1} TEV protease at 25 °C overnight. Proteins were centrifuged at 13,000*g* for 10 min, the supernatant was discarded, and the protein was washed and remixed with dialysis buffer. The same process was repeated three times. The LCD alone was then dissolved in buffer containing 20 mM Mops, pH 7.5, 150 mM KCl buffer and 2 M GnCl to a final concentration of 4 to 5 mg ml^{-1}. Samples then were shaken at 4 °C for 3 days using a digital dry bath (Torrey Pines Scientific) at speed 9. Fibrils presence was checked by negative-stain EM.

Negative staining transmission electron microscopy

Samples for transmission electron microscopy were prepared by applying 2.5 μl of sample on glow-discharged 400 mesh carbon-coated formvar support films mounted on copper grids (Ted Pella, Inc). The samples were allowed to adhere for 2 min, and washed twice with water. The samples were then stained for 2 min with 2% uranyl acetate and allowed to dry for 1 min. Each grid was inspected using a T12 (FEI) electron microscope.

Phase separation and "aging" experiments with ThT

Purified and concentrated mCherry-hnRNPA2-LCDs were incubated with TEV protease and washed as described in the previous section. The LCD alone was dissolved in 5.7 M GnCl, and then diluted to 100 uM GnCl using the buffer containing 20 mM Tris–HCl, pH 7.4 and 150 mM NaCl. Samples immediately turned turbid and underwent phase separation.

For the "aging" experiments, samples were put in a 96-well plate and monitored over time using a differential interference contrast microscopy (Zeiss). For phase separation with

ThT assays, 20 μM final concentration of ThT was added to the sample and monitored over time using Zeiss. The plate was imaged in phase contrast channel (differential interference contrast) with 300 ms exposure time, in the BO-PRO-1 channel (ThT) with 100 ms exposure time. BO-PRO-1 channel has an excitation and emission of 462 nm and 482 nm. All images were taken at full camera resolution without any binning. Measurements were taken at every 15 min, and representative images were presented in the main texts. Liquid droplets diameter quantification is measured using the software Nano Measure 1.2 (https://nano-measurer.software.informer.com/). Twenty droplets from each image, with a total of 10 images and 200 droplets, were averaged to get the mean diameter which is representative of the whole well.

For phase separation experiments with different pHs, buffers we used are the following: 20 mM sodium acetate, pH 1.3 and 150 mM NaCl; 20 mM sodium acetate with acetic acid, pH 4.1 and 150 mM NaCl; 20 mM sodium acetate with acetic acid, pH 5.5 and 150 mM NaCl; 20 mM Tris–HCl, pH 7.5 and 150 mM NaCl; 20 mM Ches, pH 9.0 and 150 mM NaCl; 20 mM Ches, pH 10.0 and 150 mM NaCl.

For liquid droplet thermostability assays, phase separation was formed in the 96-well plate and sat at 25 °C for 24 h. The plate was then incubated at 37 °C for an hour and stirred with pipette. The 96-well plate was then incubated at 4 °C overnight, and stirred with pipette the next day. Sample status was checked and recorded using Zeiss.

Thermostability assays of hnRNPA2 LCD fibrils

Both the WT and the mutant hnRNPA2 LCD alone fibrils were heated up from 4 °C to 95 °C with a 10 °C increment, and at each temperature, samples were incubated for 15 min in a PCR machine. A total of 2.5 μl of samples at each temperature were taken and checked by negative stain EM. After heating at 95 °C for 15 min, the samples were incubated at 4 °C overnight and then checked by negative stain EM.

Cryo-EM data collection, reconstruction, and model building

A total of 2.5 μl of hnRNPA2 LCD alone fibrils at a concentration of 4 mg ml^{-1} were applied to glow-discharged Quantifoil Cu R 1.2/1.3, 300 mesh carbon grids. Samples were blotted with filter paper to remove excess sample and then plunge-frozen in liquid ethane using a Vitrobot Mark IV (FEI). Cryo-EM data were collected on a Gatan K2 Summit direct electron detector on a Titan Krios (FEI) microscope equipped with a Gatan Quantum LS/K2 Summit direct electron detection camera (operated with 300 kV acceleration voltage and slit width of 20 eV). Super-resolution movies were acquired with a pixel size of 1.1 Å $pixel^{-1}$ (0.55 Å $pixel^{-1}$ in super-resolution movie frame). Thirty movie frames were recorded each with a frame rate of 5 Hz using a dose rate of 1.2 e^{-} $Å^{-2}$ $frame^{-1}$ for a final dose of 36 e^{-} $Å^{-2}$ on the sample. Automated data collection was driven by the Leginon automation software (https://emg.nysbc.org/redmine/projects/leginon/wiki/Leginon_Homepage) package (47). A total of 4366 micrographs were collected with a defocus range from 0.5 to 5.0 μm.

Unblur (48) was used to correct beam-induced motion with dose weighting and anisotropic magnification correction, leading to a physical pixel size of 1.064 Å $pixel^{-1}$. Micrographs summing all frames were all corrected for gain reference, and then micrographs with a group of three frames were used to estimate the contrast transfer function using CTFFIND 4.1.8 (https://grigoriefflab.umassmed.edu/ctffind4) (49). Micrographs with crystalline ice, severe astigmatism, or obvious drift were discarded. All subsequent data processing was performed using RELION 3.1.1 (https://relion.readthedocs.io/en/release-5.0/) (50, 51).

All filaments were picked using crYOLO (https://cryolo.readthedocs.io/en/stable/) (52), trained with 100 micrographs we picked manually using EMAN2 e2helixboxer.py (53). Particles were first extracted using a box size of 1024 and 686 pixels with an interbox distance of 10% of the box length. 2D classification using 1024-pixel particles was used to estimate the fibril pitch and helical parameters. We also performed 2D classifications with 686-pixel particles to select particles for future 3D classification. We performed Class3D jobs with three classes and manually controlled the tau_fudge factor and healpix_order to obtain resolutions around 8 to 9 Å, using an elongated Gaussian blob as an initial reference. We selected particles that contribute to the highest resolution class and generated an initial 3D reconstruction by running Class3D with 1 class. To obtain a higher resolution reconstruction, we reextracted particles with a box size of 320 pixels from the fibril tubes containing the Class3D-selected 686-pixel particles. All 320-pixel particles were used directly for 3D classifications. The final subset of selected particles was used for high-resolution gold-standard refinement as described previously (51). We apply a lowpass filter of 40 Å (–ini_high 40). The final overall resolution estimates for PM1-3 were evaluated to be 3.3 Å, 3.2 Å, and 3.9 Å, respectively, based on the 0.143 Fourier shell correlation (FSC) cutoff (54). Projections from the final reconstruction closely match the 2D class averages, helping to validate the reconstruction.

The refined map was sharpened using phenix.auto_sharpen at the resolution cutoff (55), and a near-atomic resolution model was built *de novo* into the sharpened map using COOT (56). We generated a five-layer model using the helical parameters from the final 3D refinement and then refined the structure using phenix.real_space_refine (57). After the last round of refinement, the final model was validated using phenix.comprehensive_validation (58, 59). The same protocols were performed for all three PMs. All the statistics are summarized in Table 1.

Atomic solvation energy calculations

The solvation energy was calculated as described previously (26, 60). The solvation energy for each residue was calculated by the sum of the products of the area buried for each atom and the corresponding atomic solvation parameters. The overall energy was calculated by the sum of energies of all residues. Different colors were assigned to each residue, instead of each atom, in the solvation energy map. The energy reported for FUS is the average over 20 NMR models.

Data availability

All data needed to evaluate the conclusions in the paper are present in the paper and/or the Supplementary Materials. Additional data related to this paper may be requested from the authors. The cryo-EM density maps of PM1-3 of the D290V mutant of hnRNPA2 have been deposited in the Electron Microscopy Data Bank under the accession code EMDB-27713, EMDB-27728, and EMDB-28014 respectively. The resulting atomic models have been deposited in the Protein Data Bank under the accession code PDB-8DU2, PDB-8DUW, and PDB-8EC7, respectively.

Supporting information—This article contains supporting information.

Acknowledgments—We are grateful to Dr Masato Kato and Dr Steven L. McKnight from University of Texas, Southwestern Medical Center for sending us the construct of mCherry-hnRNPA2-LCD and their advice on sample preparation. We thank Lukasz Salwinski for his help in cloning. We acknowledge the use of instruments at the EICN supported by the California NanoSystems Institute at the University of California, Los Angeles. The authors acknowledge NIH Grants 1RF1AG065407, 1R01AG070895, and R01 AG048120, and NSF Grant MCB 1616265, and Department of Energy Grant DE-FC02-02ER63421 for support.

Author contributions—J. L., P. G., Q. C., and D. R. B. formal analysis; J. L. and P. G. validation; J. L., M. R. S., M. P. H., D. R. B., and D. S. E. writing–review and editing; J. L. and M. R. S., visualization; J. L. and M. P. H. conceptualization; J. L. and D. S. E. project administration; J. L. methodology; J. L., investigation; J. L. writing–original draft; P. G., M. R. S., D. C., and M. P. H. software; D. C., R. A., and E. T.-F. resources; D. S. E. supervision; D. S. E. funding acquisition.

Funding and additional information—J. L. was supported by the Audree V. Fowler fellowship in Protein Science and Dissertation Year Fellowship. The content is solely the responsibility of the authors and does not necessarily represent the official views of the National Institutes of Health.

Conflict of interest—D. S. E. is an advisor and equity shareholder in ADRx, Inc.

Abbreviations—The abbreviations used are: FUS, fused in sarcoma; GnCl, guanidinium hydrochloride; hnRNPA2, heterogeneous nuclear ribonucleoprotein A2; LARKS, low-complexity, amyloid-like, reversible, kinked segments; LCD, low complexity domain; MLOs, membraneless organelles; MSP, multisystem proteinopathy; NLS, nuclear localization signal; TCEP, tris(2-carboxyethyl)phosphine; TDP, TAR DNA-binding protein; TEV, tobacco etch virus; ThT, thioflavin-T.

References

1. Korb, M. K., Kimonis, V. E., and Mozaffar, T. (2021) Multisystem proteinopathy: where myopathy and motor neuron disease converge. *Muscle Nerve* **63**, 442–454
2. Watts, G. D. J., Wymer, J., Kovach, M. J., Mehta, S. G., Mumm, S., Darvish, D., *et al.* (2004) Inclusion body myopathy associated with Paget disease of bone and frontotemporal dementia is caused by mutant valosin-containing protein. *Nat. Genet.* **36**, 377–381
3. Kim, H. J., Kim, N. C., Wang, Y. D., Scarborough, E. A., Moore, J., Diaz, Z., *et al.* (2013) Mutations in prion-like domains in hnRNPA2B1 and hnRNPA1 cause multisystem proteinopathy and ALS. *Nature* **495**, 467–473
4. Patel, A., Lee, H. O., Jawerth, L., Maharana, S., Jahnel, M., Hein, M. Y., *et al.* (2015) A liquid-to-solid phase transition of the ALS protein FUS accelerated by disease mutation. *Cell* **162**, 1066–1077
5. Salajegheh, M., Pinkus, J. L., Taylor, J. P., Amato, A. A., Nazareno, R., Baloh, R. H., and Greenberg, S. A. (2009) Sarcoplasmic redistribution of nuclear TDP-43 in inclusion body myositis. *Muscle Nerve* **40**, 19–31
6. Fonda, B. D., Jami, K. M., Boulos, N. R., and Murray, D. T. (2021) Identification of the rigid core for aged liquid droplets of an RNA-binding protein low complexity domain. *J. Am. Chem. Soc.* **143**, 6657–6668
7. Ryan, V. H., Watters, S., Amaya, J., Khatiwada, B., Venditti, V., Naik, M. T., and Fawzi, N. L. (2020) Weak binding to the A2RE RNA rigidifies hnRNPA2 RRMs and reduces liquid–liquid phase separation and aggregation. *Nucleic Acids Res.* **48**, 10542–10554
8. Liu, Y., and Shi, S. L. (2021) The roles of hnRNP A2/B1 in RNA biology and disease. *Wiley Interdiscip Rev. RNA* **12**, e1612
9. White, R., Gonsior, C., Krämer-Albers, E. M., Stöhr, N., Hüttelmaier, S., and Trotter, J. (2008) Activation of oligodendroglial Fyn kinase enhances translation of mRNAs transported in hnRNP A2-dependent RNA granules. *J. Cell Biol.* **181**, 579–586
10. Amaya, J., Ryan, V. H., and Fawzi, N. L. (2018) The SH3 domain of Fyn kinase interacts with and induces liquid–liquid phase separation of the low-complexity domain of hnRNPA2. *J. Biol. Chem.* **293**, 19522–19531
11. Ryan, V. H., Dignon, G. L., Zerze, G. H., Chabata, C. V., Silva, R., Conicella, A. E., *et al.* (2018) Mechanistic view of hnRNPA2 low-complexity domain structure, interactions, and phase separation altered by mutation and arginine methylation. *Mol. Cell* **69**, 465–479.e7
12. Conicella, A. E., Dignon, G. L., Zerze, G. H., Schmidt, H. B., D'Ordine, A. M., Kim, Y. C., *et al.* (2020) TDP-43 α-helical structure tunes liquid–liquid phase separation and function. *Proc. Natl. Acad. Sci.* **117**, 5883–5894
13. Ding, X., Gu, S., Xue, S., and Luo, S.-Z. (2021) Disease-associated mutations affect TIA1 phase separation and aggregation in a proline-dependent manner. *Brain Res.* **1768**, 147589
14. Wheeler, J. R., Matheny, T., Jain, S., Abrisch, R., and Parker, R. (2016) Distinct stages in stress granule assembly and disassembly. *eLife* **5**, e18413
15. Buratti, E., Brindisi, A., Giombi, M., Tisminetzky, S., Ayala, Y. M., and Baralle, F. E. (2005) TDP-43 binds heterogeneous nuclear ribonucleoprotein A/B through its C-terminal tail: an important region for the inhibition of cystic fibrosis transmembrane conductance regulator exon 9 splicing. *J. Biol. Chem.* **280**, 37572–37584
16. Qi, X., Pang, Q., Wang, J., Zhao, Z., Wang, O., Xu, L., *et al.* (2017) Familial early-onset Paget's disease of bone associated with a novel hnRNPA2B1 mutation. *Calcif. Tissue Int.* **101**, 159–169
17. Forman-Kay, J. D., Kriwacki, R. W., and Seydoux, G. (2018) Phase separation in biology and disease. *J. Mol. Biol.* **430**, 4603–4606
18. Lu, J., Cao, Q., Hughes, M. P., Sawaya, M. R., Boyer, D. R., Cascio, D., and Eisenberg, D. S. (2020) CryoEM structure of the low-complexity domain of hnRNPA2 and its conversion to pathogenic amyloid. *Nat. Commun.* **11**, 4090
19. Hughes, M. P., Sawaya, M. R., Boyer, D. R., Goldschmidt, L., Rodriguez, J. A., Cascio, D., *et al.* (2018) Atomic structures of low-complexity protein segments reveal kinked β sheets that assemble networks. *Science* **359**, 698–701
20. Xiang, S., Kato, M., Wu, L. C., Lin, Y., Ding, M., Zhang, Y., *et al.* (2015) The LC domain of hnRNPA2 adopts similar conformations in hydrogel polymers, liquid-like droplets and nuclei. *Cell* **163**, 829–839
21. Kato, M., Han, T. W., Xie, S., Shi, K., Du, X., Wu, L. C., *et al.* (2012) Cell-free formation of RNA granules: low complexity sequence domains form dynamic fibers within hydrogels. *Cell* **149**, 753–767
22. Goldschmidt, L., Teng, P. K., Riek, R., and Eisenberg, D. (2010) Identifying the amylome, proteins capable of forming amyloid-like fibrils. *Proc. Natl. Acad. Sci. U. S. A.* **107**, 3487–3492

23. Biancalana, M., and Koide, S. (2010) Molecular mechanism of Thioflavin-T binding to amyloid fibrils. *Biochim. Biophys. Acta* **1804**, 1405–1412
24. Springhower, C. E., Rosen, M. K., and Chook, Y. M. (2020) Karyopherins and condensates. *Curr. Opin. Cell Biol.* **64**, 112–123
25. Sawaya, M. R., Sambashivan, S., Nelson, R., Ivanova, M. I., Sievers, S. A., Apostol, M. I., *et al.* (2007) Atomic structures of amyloid cross-beta spines reveal varied steric zippers. *Nature* **447**, 453–457
26. Sawaya, M. R., Hughes, M. P., Rodriguez, J. A., Riek, R., and Eisenberg, D. S. (2021) The expanding amyloid family: structure, stability, function, and pathogenesis. *Cell* **184**, 4857–4873
27. Murray, D. T., Zhou, X., Kato, M., Xiang, S., Tycko, R., and McKnight, S. L. (2018) Structural characterization of the D290V mutation site in hnRNPA2 low-complexity-domain polymers. *Proc. Natl. Acad. Sci. U. S. A.* **115**, E9782–E9791
28. Lu, J., Yu, Y., Zhu, I., Cheng, Y., and Sun, P. D. (2014) Structural mechanism of serum amyloid A-mediated inflammatory amyloidosis. *Proc. Natl. Acad. Sci. U. S. A.* **111**, 5189–5194
29. Fitzpatrick, A. W. P., Falcon, B., He, S., Murzin, A. G., Murshudov, G., Garringer, H. J., *et al.* (2017) Cryo-EM structures of tau filaments from Alzheimer's disease. *Nature* **547**, 185–190
30. Murray, D. T., Kato, M., Lin, Y., Thurber, K. R., Hung, I., McKnight, S. L., and Tycko, R. (2017) Structure of FUS protein fibrils and its relevance to self-assembly and phase separation of low-complexity domains. *Cell* **171**, 615–627.e16
31. Zhang, Z. C., and Chook, Y. M. (2012) Structural and energetic basis of ALS-causing mutations in the atypical proline–tyrosine nuclear localization signal of the Fused in Sarcoma protein (FUS). *Proc. Natl. Acad. Sci. U. S. A.* **109**, 12017–12021
32. Soniat, M., Sampathkumar, P., Collett, G., Gizzi, A. S., Banu, R. N., Bhosle, R. C., *et al.* (2013) Crystal structure of human Karyopherin β2 bound to the PY-NLS of Saccharomyces cerevisiae Nab2. *J. Struct. Funct. Genomics* **14**, 31–35
33. Imasaki, T., Shimizu, T., Hashimoto, H., Hidaka, Y., Kose, S., Imamoto, N., *et al.* (2007) Structural basis for substrate recognition and dissociation by human transportin 1. *Mol. Cell* **28**, 57–67
34. Cansizoglu, A. E., Lee, B. J., Zhang, Z. C., Fontoura, B. M. A., and Chook, Y. M. (2007) Structure-based design of a pathway-specific nuclear import inhibitor. *Nat. Struct. Mol. Biol.* **14**, 452–454
35. Lee, B. J., Cansizoglu, A. E., Süel, K. E., Louis, T. H., Zhang, Z., and Chook, Y. M. (2006) Rules for nuclear localization sequence recognition by Karyopherinβ2. *Cell* **126**, 543–558
36. Soniat, M., and Chook, Y. M. (2016) Karyopherin-β2 recognition of a PY-NLS variant that lacks the proline-tyrosine motif. *Structure* **24**, 1802–1809
37. Kim, H. J., Mohassel, P., Donkervoort, S., Guo, L., O'Donovan, K., Coughlin, M., *et al.* (2022) Heterozygous frameshift variants in HNRNPA2B1 cause early-onset oculopharyngeal muscular dystrophy. *Nat. Commun.* **13**, 2306
38. Boyer, D. R., Li, B., Sun, C., Fan, W., Zhou, K., Hughes, M. P., *et al.* (2020) The α-synuclein hereditary mutation E46K unlocks a more stable, pathogenic fibril structure. *Proc. Natl. Acad. Sci. U. S. A.* **117**, 3592–3602
39. Muslimov, I. A., Tuzhilin, A., Tang, T. H., Wong, R. K. S., Bianchi, R., and Tiedge, H. (2014) Interactions of noncanonical motifs with hnRNP A2 promote activity-dependent RNA transport in neurons. *J. Cell Biol.* **205**, 493–510
40. Kamma, H., Fujimoto, M., Fujiwara, M., Matsui, M., Horiguchi, H., Hamasaki, M., and Satoh, H. (2001) Interaction of hnRNP A2/B1 isoforms with telomeric ssDNA and the *in vitro* function. *Biochem. Biophys. Res. Commun.* **280**, 625–630
41. Nguyen, E. D., Balas, M. M., Griffin, A. M., Roberts, J. T., and Johnson, A. M. (2018) Global profiling of hnRNP A2/B1-RNA binding on chromatin highlights LncRNA interactions. *RNA Biol.* **15**, 901–913
42. Guerrero-Ferreira, R., Taylor, N. M., Arteni, A. A., Kumari, P., Mona, D., Ringler, P., *et al.* (2019) Two new polymorphic structures of human full-length alpha-synuclein fibrils solved by cryo-electron microscopy. *eLife* **8**, e48907
43. Cao, Q., Boyer, D. R., Sawaya, M. R., Abskharon, R., Saelices, L., Nguyen, B. A., *et al.* (2021) Cryo-EM structures of hIAPP fibrils seeded by patient-extracted fibrils reveal new polymorphs and conserved fibril cores. *Nat. Struct. Mol. Biol.* **28**, 724–730
44. Tycko, R. (2015) Amyloid polymorphism: structural basis and neurobiological relevance. *Neuron* **86**, 632–645
45. Li, B., Ge, P., Murray, K. A., Sheth, P., Zhang, M., Nair, G., *et al.* (2018) Cryo-EM of full-length α-synuclein reveals fibril polymorphs with a common structural kernel. *Nat. Commun.* **9**, 3609
46. Babinchak, W. M., Haider, R., Dumm, B. K., Sarkar, P., Surewicz, K., Choi, J. K., and Surewicz, W. K. (2019) The role of liquid–liquid phase separation in aggregation of the TDP-43 low-complexity domain. *J. Biol. Chem.* **294**, 6306–6317
47. Suloway, C., Pulokas, J., Fellmann, D., Cheng, A., Guerra, F., Quispe, J., *et al.* (2005) Automated molecular microscopy: the new Leginon system. *J. Struct. Biol.* **151**, 41–60
48. Grant, T., and Grigorieff, N. (2015) Measuring the optimal exposure for single particle cryo-EM using a 2.6 Å reconstruction of rotavirus VP6. *eLife* **4**, e06980
49. Rohou, A., and Grigorieff, N. (2015) CTFFIND4: fast and accurate defocus estimation from electron micrographs. *J. Struct. Biol.* **192**, 216–221
50. He, S., and Scheres, S. H. W. (2017) Helical reconstruction in RELION. *J. Struct. Biol.* **198**, 163–176
51. Scheres, S. H. W. (2012) RELION: implementation of a Bayesian approach to cryo-EM structure determination. *J. Struct. Biol.* **180**, 519–530
52. Wagner, T., Lusnig, L., Pospich, S., Stabrin, M., Schönfeld, F., and Raunser, S. (2020) Two particle-picking procedures for filamentous proteins: SPHIRE-crYOLO filament mode and SPHIRE-STRIPER. *Acta Crystallogr. Sect. Struct. Biol.* **76**, 613–620
53. Tang, G., Peng, L., Baldwin, P. R., Mann, D. S., Jiang, W., Rees, I., and Ludtke, S. J. (2007) EMAN2: an extensible image processing suite for electron microscopy. *J. Struct. Biol.* **157**, 38–46
54. Chen, S., McMullan, G., Faruqi, A. R., Murshudov, G. N., Short, J. M., Scheres, S. H. W., and Henderson, R. (2013) High-resolution noise substitution to measure overfitting and validate resolution in 3D structure determination by single particle electron cryomicroscopy. *Ultramicroscopy* **135**, 24–35
55. Terwilliger, T. C., Sobolev, O. V., Afonine, P. V., and Adams, P. D. (2018) Automated map sharpening by maximization of detail and connectivity. *Acta Crystallogr. Sect. Struct. Biol.* **74**, 545–559
56. Emsley, P., Lohkamp, B., Scott, W. G., and Cowtan, K. (2010) Features and development of Coot. *Acta Crystallogr. D Biol. Crystallogr.* **66**, 486–501
57. Afonine, P. V., Poon, B. K., Read, R. J., Sobolev, O. V., Terwilliger, T. C., Urzhumtsev, A., and Adams, P. D. (2018) Real-space refinement in PHENIX for cryo-EM and crystallography. *Acta Crystallogr. Sect. Struct. Biol.* **74**, 531–544
58. Adams, P. D., Afonine, P. V., Bunkóczi, G., Chen, V. B., Davis, I. W., Echols, N., *et al.* (2010) PHENIX: a comprehensive Python-based system for macromolecular structure solution. *Acta Crystallogr. D Biol. Crystallogr.* **66**, 213–221
59. Chen, V. B., Arendall, W. B., Headd, J. J., Keedy, D. A., Immormino, R. M., Kapral, G. J., *et al.* (2010) MolProbity: all-atom structure validation for macromolecular crystallography. *Acta Crystallogr. D Biol. Crystallogr.* **66**, 12–21
60. Eisenberg, D., Wesson, M., and Yamashita, M. (1989) Interpretation of protein folding and binding with atomic solvation parameters. *Chemica Scripta* **29A**, 217–222